Title

Understanding the Structural Evolution of IrFeCoNiCu High-Entropy Alloy Nanoparticles under the Acidic Oxygen Evolution Reaction

Journal

Nano Letters, 23(14)

ISSN

1530-6984

Authors

Maulana, Arifin Luthfi
Chen, Peng-Cheng
Shi, Zixiao
et al.

Publication Date

2023-07-26

DOI

10.1021/acs.nanolett.3c01831

Peer reviewed

Understanding the Structural Evolution of IrFeCoNiCu High-Entropy Alloy Nanoparticles under Acidic Oxygen Evolution Reaction

Arifin Luthfi Maulana[1,2,†], Peng-Cheng Chen[2,3,4,†,‡], Zixiao Shi[5,6], Yao Yang[4,7], Carlos Lizandara-Pueyo[2], Fabian Seeler[8], Héctor D. Abruña[5], David Muller[6,9], Kerstin Schierle-Arndt[8], Peidong Yang[1,2,3,4,*]

[1]Department of Materials Science and Engineering, University of California, Berkeley, Berkeley, California 94720, United States.

[2]California Research Alliance (CARA), BASF Corporation, Berkeley, California 94720, United States.

[3]Kavli Energy Nanoscience Institute, University of California, Berkeley, Berkeley, California 94720, United States.

[4]Department of Chemistry, University of California, Berkeley, Berkeley, California 94720, United States.

[5]Department of Chemistry and Chemical Biology, Cornell University, Ithaca, New York 14850, United States.

[6]School of Applied and Engineering Physics, Cornell University, Ithaca, New York 14850, United States.

[7]Miller Institute for Basic Research in Science, University of California, Berkeley, Berkeley, California 94720, United States.

[8]BASF SE, 67056 Ludwigshafen am Rhein, Germany.

[9]Kavli Institute at Cornell for Nanoscale Science, Cornell University, Ithaca 14850, New York, United States.

‡ Present address: Department of Materials Science, Fudan University, Shanghai 200438, China.

*Corresponding author. Email: p_yang@berkeley.edu

†These authors contributed equally to this work.

Abstract:

High-entropy alloy (HEA) nanoparticles are promising catalyst candidates for the acidic oxygen evolution reaction (OER). Herein, we report the synthesis of IrFeCoNiCu-HEA nanoparticles on carbon paper substrate *via* microwave-assisted shock synthesis method. Under OER conditions in 0.1 M $HClO_4$, the HEA nanoparticles exhibit excellent activity with an overpotential of ~302 mV measured at 10 mA cm^{-2} and improved stability over 12 hours of operation compared to the monometallic Ir counterpart. Importantly, an active Ir-rich shell layer with nano-domain features was observed to form on the surface of IrFeCoNiCu-HEA nanoparticles immediately after undergoing electrochemical activation, mainly due to the dissolution of the constituent 3*d* metals. The core of the particles was able to preserve the characteristic homogeneous single-phase HEA structure without significant phase separation or elemental segregation. This work illustrates that under operating acidic conditions, the near-surface structure of HEA nanoparticles is susceptible to a certain degree of structural dynamics.

Keywords: *High-entropy alloy; acidic OER; structural evolution; dissolution.*

Main Text

Electrochemical water splitting in acidic media realized using renewable electricity is an important pathway for the decarbonization of large-scale hydrogen (H_2) production.[1–5] However, the oxygen evolution reaction (OER) as the anode half-cell reaction hampers the widespread use of efficient proton-exchange membrane water electrolyzers, mainly due to its sluggish kinetics and harsh reaction environment.[5–6] While IrO_2 and RuO_2 as state-of-the-art catalysts are active for acidic OER,[7–8] their long-term stability under OER is still insufficient due to the dissolution of Ir and Ru.[9–14] Therefore, there is a pressing need to develop an OER catalyst with improved activity and enhanced stability to achieve a more efficient water-splitting process.

High-entropy alloy (HEA) nanoparticles are promising nanomaterials that provide tremendous opportunities for various fields, including catalysis.[15–18] The considerable configurational entropy generated by incorporating five or more elements into a single particle, in principle, can dominate the particle's thermodynamic behavior, stabilize the alloyed structure, and even mitigate structural degradation under unrelenting conditions.[15] In addition, HEA manifests a mixing effect, resulting in synergistic responses from the mutual electronic interactions between its constituent elements.[16–18] The availability of multi-element active sites on the HEA nanoparticle surface also makes HEA suitable for catalytic reactions, including OER.[19–22] However, the exploration of HEA as a catalyst in acidic OER environments is relatively underexplored,[23–26] as most studies focus on alkaline electrolytes.[27–29]

Our work focuses on developing Ir-based HEA nanoparticles as efficient catalysts for acidic OER. Using microwave-assisted shock synthesis, we successfully synthesized IrFeCoNiCu-HEA, which outperforms monometallic Ir and other Ir-based bimetallic alloys, such as IrFe, IrCo, and IrNi. Immediately upon OER electrochemical activation, the HEA undergoes a structural evolution, forming a relatively stable structure with an active Ir-rich shell layer on the nanoparticle surface, mainly due to the dissolution of the constituent 3*d* metals (Fe, Co, Ni, and Cu) under highly acidic and oxidative condition. Meanwhile, the nanoparticle's core maintains a homogeneous elemental distribution characteristic of an HEA structure. Our results show that this evolved structure is stable during at least 12 hours of chronopotentiometry test without excessive activity degradation, demonstrating the prospect of Ir-based HEA nanoparticles as active and stable OER catalysts.

IrFeCoNiCu-HEA nanoparticles were prepared using a microwave-assisted shock synthesis method (for experimental details, see the Methods section in the Supporting Information (SI)). Rapid heating and rapid quenching from microwave irradiation are advantageous in synthesizing nanoscale single-phase alloyed structures.[30–32] IrFeCoNiCu-HEA nanoparticles can be dispersed on the carbon paper substrate with nanoparticles size distributed between 20 and 200 nm (Figures 1a and S1). The vast particle size distribution is presumably caused by the inhomogeneity of the carbon paper substrate and different heating conditions delivered by the microwave setup for different batches of synthesis. High-angle annular dark-field scanning transmission electron microscopy (HAADF-STEM) and powder X-ray diffraction (XRD) studies were conducted to elucidate the structure of the synthesized HEA. HAADF-STEM image (Figure 1b) and the corresponding fast Fourier transform (FFT) analysis (inset on Figure 1b) show the {111} and {200} lattice planes, respectively, viewed along the [110] zone axis. Based on the lattice structure analysis, the HEA is observed to assume a typical metallic FCC structure. The XRD pattern (Figure 1c) also supports this crystal structure claim. The single set of FCC diffraction peaks indicates that IrFeCoNiCu-HEA nanoparticles have a dominant single-phase structure without any apparent additional phases. Compared to the XRD pattern of each component, the peaks of IrFeCoNiCu-HEA do not belong to any of the monometallic elements, indicating a homogeneous mixing between all elements. The average lattice constant calculated from XRD measurements is 0.364 nm. The atomic ratio at a whole sample level was measured using inductively coupled plasma optical emission spectroscopy (ICP-OES), as listed in Table S1. The measured Ir:Fe:Co:Ni:Cu atomic ratio (19:19:20:22:21) is observed to be near-equimolar and conforms well with the definition of an HEA at the bulk level.[33] With the experimentally measured ratio, the estimated lattice constant predicted using ideal Vegard's law is 0.369 nm, consistent with the calculated value from XRD measurements.

The single-phase solid solution alloy structure of IrFeCoNiCu-HEA is further confirmed by STEM energy dispersive spectroscopy (STEM-EDX) elemental mapping (Figures 1d and S2). The elemental distribution maps show a homogeneous distribution of each component without any significant phase separation or elemental segregation. From the STEM-EDX spectra of selected regions of interest, both at an ensemble (Figure S2) and at a single particle level (Figure S3), the typical atomic ratio between Ir:Fe:Co:Ni:Cu was calculated to be also near equimolar. In addition,

the random mixing of the elements can also be confirmed by the *Z*-contrast-based HAADF-STEM images of this nanoparticle at the atomic scale (Figures 1b and S4).

After studying the structure and composition of the as-synthesized IrFeCoNiCu-HEA, we performed electrochemical OER measurements to evaluate its electrocatalytic activity and stability in acidic media. The measurements were carried out using a three-electrode system in an H-cell using 0.1 M $HClO_4$ electrolyte. Figure 2a depicts the OER polarization curve of a blank carbon paper, monometallic Ir, IrM (M = Fe, Co, Ni) bimetallic alloys, and IrFeCoNiCu-HEA. IrFeCoNiCu-HEA exhibits an enhanced activity with an overpotential measured of about 302 mV at 10 mA cm^{-2}, while the overpotential of pure Ir catalyst with similar Ir-mass loading (~288 μg_{Ir} $cm^{-2}_{geo.}$) is about 352 mV. As an additional activity comparison, OER tests were also performed on IrFe, IrCo, and IrNi catalysts. These catalysts have been widely reported to exhibit excellent OER performance in acidic media compared to pure Ir and the state-of-the-art IrO_2 catalyst.[34–40] These bimetallic catalysts were prepared in a similar fashion to that of IrFeCoNiCu-HEA with equal Ir-mass loading (Figure S5). Compared to these catalysts, IrFeCoNiCu-HEA also shows better OER activity, further signifying the excellent performance of this HEA. The OER kinetics on IrFeCoNiCu-HEA nanoparticles are also improved, showed by the Tafel slope of about 58.0 mV dec^{-1} for the IrFeCoNiCu-HEA, which is lower than that of pure Ir (about 75.8 mV dec^{-1}) and other IrM bimetallic systems, as presented in Figure 2b.

The activity of IrFeCoNiCu-HEA and monometallic Ir was also compared by normalizing the current density with Ir-mass loading and electrochemically active surface area (ECSA) measured using the hydrogen underpotential deposition (H_{UPD}) region. With similar Ir-mass loading, IrFeCoNiCu-HEA demonstrates a better Ir-mass-based activity compared to pure Ir catalyst (Figures 2c and S6). At 300 mV overpotential, the activity of IrFeCoNiCu-HEA (34.67 A g^{-1}_{Ir}) is about 2.2 times better than that of pure Ir (15.76 A g^{-1}_{Ir}). We then measured the ECSA for IrFeCoNiCu-HEA and pure Ir to be about 4.75 m^2 g^{-1}_{Ir} and 4.30 m^2 g^{-1}_{Ir}, respectively. When normalized to the ECSA, IrFeCoNiCu-HEA exhibits activity 1.9 times better than pure Ir catalyst at 300 mV overpotential (Figure S7). The OER stability of the catalysts was evaluated using chronopotentiometry tests at a constant current density of 10 mA cm^{-2} for up to 12 hours.[41–43] As indicated in Figure 2d, IrFeCoNiCu-HEA sustains better OER stability compared to pure Ir. After 12 hours, the overpotential increase measured from the chronopotentiometry test for IrFeCoNiCu-HEA is less than 60 mV, while for pure Ir is up to 120 mV. In addition, a study conducted by Cai

et al. showed that the same elemental combination also exhibits improved OER activity in an alkaline environment.[27]

It should be noted that during the synthesis process, we observed the existence of carbon layers encapsulating the HEA nanoparticles with a thickness of about 5 nm (Figures S9a and S9b). The encapsulating layers have been reported to be formed on typical processes that involve heat treatment of nanoparticles on different types of carbon substrates.[44] The presence of carbon layers has been widely debated for its effect in enhancing the activity and durability of Pt-based nanomaterials for oxygen reduction reaction (ORR) as it blocks the active Pt sites.[45] However, in the case of our synthesized IrFeCoNiCu-HEA, we observed that the carbon layers were delaminated after undergoing electrochemical activation (Figures S9c-S9f), indicating the negligible effects of carbon layers on the activity and stability of the catalyst.

After evaluating the activity and stability of the catalysts, the structural evolution of IrFeCoNiCu-HEA before and after OER experiments were then analyzed. Investigation into the structural transformation of HEA catalysts is often neglected but instrumental in understanding the behavior of HEA catalysts under catalytic environments. Notably, *in situ* studies by Song *et al.* provide valuable insights into probing the behavior of HEA nanoparticles under air and hydrogen atmospheres.[46–47] Here, we show evidence of structural evolution in IrFeCoNiCu-HEA under acidic OER conditions. Figure 3a depicts the *ex situ* STEM-EDX maps of each element, a composite map between Ir and Ni, and the overlay map of all elements of different IrFeCoNiCu-HEA samples collected after different treatments. The purpose of superimposing Ir and Ni elemental maps is to provide better color contrast. The top row lists the elemental maps of as-synthesized IrFeCoNiCu-HEA before undergoing OER experiments. The middle row of Figure 3a shows the maps of an IrFeCoNiCu-HEA nanoparticle after undergoing initial cyclic voltammetry (CV) for electrochemical activation and linear-sweep voltammetry (LSV) for activity measurement. From the composite Ir + Ni and the overlay map, an Ir-rich shell layer was detected to form on the surface of the nanoparticles with a measured average thickness of about 2-6 nm. Meanwhile, the core of the nanoparticles was found to still preserve the characteristic homogeneous elemental distribution of the HEA without noticeable phase separation or elemental segregation. The average thickness of the Ir-rich shell is found to not increase significantly in samples collected after undergoing 4 hours (Figure S10a), 8 hours (Figure S10b), and 12 hours of

chronopotentiometry test at 10 mA cm^{-2} (bottom row of Figure 3a). This suggests that the evolved structure is relatively stable and does not undergo any further dramatic structural decay.

To further elucidate the driving force of this structural evolution phenomenon, we measured the concentration of the dissolved metals in the electrolyte collected from different time points using ICP-OES through *ex situ* offline measurements (Figure S11).[48] The result indicates that the dissolution process had already taken place immediately after the electrochemical activation step. The dissolved 3*d* metals were detected to have a much higher concentration than Ir due to their lower oxidation potential. The 3*d* metals and a small portion of Ir atoms occupying near the surface of the nanoparticles were leached away into the electrolyte, thus forming the Ir-rich shell layer. Such a dissolution process is widely known in OER catalysts, including Ir-based materials.[12–14,49–50] The concentration of the dissolved metals was found to not increase significantly after the initial dissolution process, as indicated by the similar concentration measured after 4 and 12 hours of chronopotentiometry measurement. This implies that the dissolution process occurs primarily during the electrochemical activation step. The dissolution during the stability test is relatively negligible. It also corroborates the finding that the average thickness of the Ir-rich shell layer does not increase significantly, even after 12 hours of the stability test. The presence of the Ir-rich shell layer might protect the core of the nanoparticle, thus lowering further dissolution of especially the 3*d* metals. It has also been reported that 3*d* metals, such as Co, in low-Ir systems can exhibit improved corrosion resistance due to their electronic structure interplay.[51]

Figure 3b displays a magnified view of the Ir-rich shell layer from a sample taken after undergoing 4 hours of chronopotentiometry test. From the individual elemental map, the shell layer is not completely absent from the existence of the 3*d* metals. The elemental distribution of Ir remains homogeneous, both in the core and near the surface of the nanoparticle. However, the elemental distribution for the 3*d* metals is seen to be more diffuse approaching the surface of the nanoparticle (illustrated by the dashed lines), implying that the core and the near-surface structure have different elemental compositions. Using this map, we further resolved the composition of the Ir-rich shell layer at different regions of interest through STEM-EDX elemental analysis (Figures S12 and S13, Table S2). At the level of the whole region, Ir largely dominates the overall composition (~31.9 at.%), surmounting the other 3*d* metals due to their dissolution after undergoing electrochemical activation. The core composition of Ir and other 3*d* metals is consistent with the typical atomic ratio of IrFeCoNiCu-HEA as previously described, suggesting

that the core still assumes the original HEA structure. On the shell layer region, the composition of Ir was measured to reach a staggering 65-75 at.%, while the rest of the composition is divided unevenly between the 3*d* metals. This denotes that the near-surface layers have lost the ability to retain the typical HEA structure with homogeneous elemental distribution when exposed to harsh acidic OER conditions. The XRD pattern of an IrFeCoNiCu-HEA sample after enduring the OER experiment is then compared to that of the as-synthesized fresh sample (Figures 3c and S14). From a more detailed inspection, the peak of the post-electrolysis sample shifts to a lower diffraction angle corresponding to a larger lattice constant. This is primarily caused by the depletion of the 3*d* metals and leaving Ir, having the largest lattice constant, to dominate the composition of the nanoparticle.

Using aberration-corrected HAADF-STEM, we resolved the morphology of the near-surface structure for samples after the electrochemical activation treatment (Figures 3d and S15). The distinction between the HEA core and the shell layer can be clearly seen here. In certain particles, the thickness of the Ir-rich shell varies from one region to another, implying that the dissolution of the metals at different parts of the nanoparticle might occur at different rates. The dissolution rate in one particle might also be different from other particles due to the particle size effect. Recalling that the synthesized IrFeCoNiCu-HEA has a broad particle size distribution, smaller-sized particles may undergo a faster surface dissolution rate due to the larger exposed surface.[52] The core of the nanoparticle is observed to still preserve the metallic HEA structure. In the shell layer, the lattice fringes can be easily recognized, indicating that this layer has a crystalline structure instead of amorphous structures. Additionally, a thin oxide layer with an average thickness of about 1 nm is detected to form on the surface of the nanoparticles, as designated by the white arrows (Figure 3d). The composition of the oxide layer has not yet been fully characterized but includes the possibility of IrO_x or a multimetallic oxide. [40,49–50,53–55] The oxide layer is found to be unevenly distributed throughout the surface of the evolved nanoparticle. STEM-EDX analysis near the surface of a nanoparticle (Figure S16a) shows the elemental distribution, including the O *K*-edge. From the line scan profile (Figure S16b), the measured average thickness of this oxide layer is about 1 nm and is consistent with the observation from the HAADF-STEM image. Electron energy-loss spectroscopy (EELS) maps and analysis (Figure S17) confirm the presence of oxygen at an appreciable concentration near the surface of the nanoparticle. However, oxygen is not only detected on the surface but also in the Ir-rich shell layer. This implies that we cannot rule out the

presence of a trace amount of oxide structures that might also form in the shell layer. Further investigation of the near-surface structure (Figures 3e and S18) demonstrates the presence of nano-domains with the crystal structure of Ir populating the shell layer and surface of the evolved nanoparticles. Figures 3f and 3g show the Ir domains having different in-plane orientations located near the surface of the nanoparticle. FFT analysis of the corresponding images confirms that these structures are mainly metallic Ir domains.

To probe the oxidation state of the near-surface structure, we performed X-ray photoelectron spectroscopy (XPS) analysis for as-synthesized and post-electrolysis IrFeCoNiCu-HEA samples. Figure S19 shows the high-resolution spectra of all the elements. Ir is found to be mainly in the metallic state with peaks at around 61.5 eV for Ir^0 $4f_{7/2}$ and 65.2 eV for Ir^0 $4f_{5/2}$. The weaker peaks at 62.7 eV and 65.6 eV can be assigned to Ir^{4+} $4f_{7/2}$ and Ir^{4+} $4f_{5/2}$, respectively.[40,56] Most of the 3d metals are found to be in their oxidized states, presumably due to their higher chemical activity.[46,56] After undergoing electrochemical activation, the Ir 4*f* spectra show a slight shift towards higher binding energy, indicating slight surface oxidation of Ir. The rest of the 3*d* metals were also observed to be mostly in their oxidized state. High-valence Ir and IrO_x have been suggested widely as the most active site in facilitating OER, which is also reasonable in the studied system since the surface structure of the evolved IrFeCoNiCu-HEA nanoparticles is mainly composed of the Ir-rich shell layer.[10,40,50,53,54] However, the contribution of the 3*d* metals near the surface of the nanoparticle in optimizing the electronic structure of the Ir site cannot be underestimated since they are observed to be not completely depleted.[40,50] Further rigorous studies are necessary to understand the active sites on such chemically complex materials, as well as the corresponding reaction mechanism. A typical four-step reaction model involving *OH, *O, and *OOH intermediates is commonly adopted for IrO_x and Ir-based multimetallic systems.[1,40,50,54,55]

Through this work, we have demonstrated the successful synthesis of IrFeCoNiCu-HEA nanoparticle catalysts via the microwave-assisted shock-synthesis method. IrFeCoNiCu-HEA exhibited an enhanced OER activity and stability compared to the monometallic Ir counterpart and other more active Ir-based bimetallic alloys. The structural evolution of IrFeCoNiCu-HEA under acidic OER operating conditions was studied. Figure 4 summarizes the general picture of the structural evolution illustrating the delamination of the encapsulating carbon layers and the dissolution of the constituent 3*d* metal atoms (Fe, Co, Ni, and Cu) from the surface of the

nanoparticle, leaving an Ir-rich shell layer, while the core maintained the homogeneous single-phase HEA structure. From this study, we suggest that high-entropy alloy nanoparticles are also susceptible to surface structural change after being exposed to harsh electrocatalytic environments (*i.e.*, highly oxidative and acidic conditions). The entropic stabilization effect near the surface of the HEA catalysts is not dominant enough to overcome the influence of electrochemical redox that occurs on the surface leading to a certain degree of surface reconstruction.

References

[1] Reier, T.; Nong, H. N.; Teschner, D.; Schlögl, R.; Strasser, P. Electrocatalytic Oxygen Evolution Reaction in Acidic Environments – Reaction Mechanisms and Catalysts. *Adv. Energy Mater.* **2017**, *7* (1), 1601275.

[2] Shi, Z.; Wang, X.; Ge, J.; Liu, C.; Xing, W. Fundamental Understanding of the Acidic Oxygen Evolution Reaction: Mechanism Study and State-of-the-Art Catalysts. *Nanoscale* **2020**, *12* (25), 13249–13275.

[3] Li, L.; Wang, P.; Shao, Q.; Huang, X. Recent Progress in Advanced Electrocatalyst Design for Acidic Oxygen Evolution Reaction. *Adv. Mater.* **2021**, *33* (50), 2004243.

[4] Marshall, A.; Børresen, B.; Hagen, G.; Tsypkin, M.; Tunold, R. Hydrogen Production by Advanced Proton Exchange Membrane (PEM) Water Electrolysers – Reduced Energy Consumption by Improved Electrocatalysis. *Energy* **2007**, *32* (4), 431–436.

[5] Suen, N.-T.; Hung, S.-F.; Quan, Q.; Zhang, N.; Xu, Y.-J.; Chen, H. M. Electrocatalysis for the Oxygen Evolution Reaction: Recent Development and Future Perspectives. *Chem. Soc. Rev.* **2017**, *46* (2), 337–365.

[6] Chen, P.-C.; Li, M.; Jin, J.; Yu, S.; Chen, S.; Chen, C.; Salmeron, M.; Yang, P. Heterostructured Au–Ir Catalysts for Enhanced Oxygen Evolution Reaction. *ACS Materials Lett.* **2021**, *3* (10), 1440–1447.

[7] Trasatti, S. Electrocatalysis by Oxides – Attempt at a Unifying Approach. *J. Electroanal. Chem. Interfacial Electrochem.* **1980**, *111* (1), 125–131.

[8] Lee, Y.; Suntivich, J.; May, K. J.; Perry, E. E.; Shao-Horn, Y. Synthesis and Activities of Rutile IrO_2 and RuO_2 Nanoparticles for Oxygen Evolution in Acid and Alkaline Solutions. *J. Phys. Chem. Lett.* **2012**, *3* (3), 399–404.

[9] Kötz, R.; Lewerenz, H. J.; Stucki, S. XPS Studies of Oxygen Evolution on Ru and RuO_2 Anodes. *J. Electrochem. Soc.* **1983**, *130* (4), 825.

[10] Kötz, R.; Neff, H.; Stucki, S. Anodic Iridium Oxide Films: XPS-Studies of Oxidation State Changes and O_2 Evolution. *J. Electrochem. Soc.* **1984**, *131* (1), 72.

[11] Antolini, E. Iridium as Catalyst and Cocatalyst for Oxygen Evolution/Reduction in Acidic Polymer Electrolyte Membrane Electrolyzers and Fuel Cells. *ACS Catal.* **2014**, *4* (5), 1426–1440.

[12] Cherevko, S.; Zeradjanin, A. R.; Topalov, A. A.; Kulyk, N.; Katsounaros, I.; Mayrhofer, K. J. J. Dissolution of Noble Metals during Oxygen Evolution in Acidic Media. *ChemCatChem* **2014**, *6* (8), 2219–2223.

[13] Cherevko, S.; Geiger, S.; Kasian, O.; Kulyk, N.; Grote, J.-P.; Savan, A.; Shrestha, B. R.; Merzlikin, S.; Breitbach, B.; Ludwig, A.; Mayrhofer, K. J. J. Oxygen and Hydrogen Evolution Reactions on Ru, RuO_2, Ir, and IrO_2 Thin Film Electrodes in Acidic and Alkaline Electrolytes: A Comparative Study on Activity and Stability. *Catal. Today* **2016**, *262*, 170–180.

[14] Danilovic, N.; Subbaraman, R.; Chang, K.-C.; Chang, S. H.; Kang, Y. J.; Snyder, J.; Paulikas, A. P.; Strmcnik, D.; Kim, Y.-T.; Myers, D.; Stamenkovic, V. R.; Markovic, N. M.

Activity–Stability Trends for the Oxygen Evolution Reaction on Monometallic Oxides in Acidic Environments. *J. Phys. Chem. Lett.* **2014**, *5* (14), 2474–2478.

[15] George, E. P.; Raabe, D.; Ritchie, R. O. High-Entropy Alloys. *Nat. Rev. Mater.* **2019**, *4* (8), 515–534.

[16] Xin, Y.; Li, S.; Qian, Y.; Zhu, W.; Yuan, H.; Jiang, P.; Guo, R.; Wang, L. High-Entropy Alloys as a Platform for Catalysis: Progress, Challenges, and Opportunities. *ACS Catal.* **2020**, *10* (19), 11280–11306.

[17] Sun, Y.; Dai, S. High-Entropy Materials for Catalysis: A New Frontier. *Sci. Adv.* **2021**, *7* (20), eabg1600.

[18] Yao, Y.; Dong, Q.; Brozena, A.; Luo, J.; Miao, J.; Chi, M.; Wang, C.; Kevrekidis, I. G.; Ren, Z. J.; Greeley, J.; Wang, G.; Anapolsky, A.; Hu, L. High-Entropy Nanoparticles: Synthesis-Structure-Property Relationships and Data-Driven Discovery. *Science* **2022**, *376* (6589), eabn3103.

[19] Batchelor, T. A. A.; Pedersen, J. K.; Winther, S. H.; Castelli, I. E.; Jacobsen, K. W.; Rossmeisl, J. High-Entropy Alloys as a Discovery Platform for Electrocatalysis. *Joule* **2019**, *3* (3), 834–845.

[20] Lu, Z.; Chen, Z. W.; Singh, C. V. Neural Network-Assisted Development of High-Entropy Alloy Catalysts: Decoupling Ligand and Coordination Effects. *Matter* **2020**, *3* (4), 1318–1333.

[21] Chen, P.-C.; Liu, X.; Hedrick, J. L.; Xie, Z.; Wang, S.; Lin, Q.-Y.; Hersam, M. C.; Dravid, V. P.; Mirkin, C. A. Polyelemental Nanoparticle Libraries. *Science* **2016**, *352* (6293), 1565–1569.

[22] Chen, P.-C.; Liu, M.; Du, J. S.; Meckes, B.; Wang, S.; Lin, H.; Dravid, V. P.; Wolverton, C.; Mirkin, C. A. Interface and Heterostructure Design in Polyelemental Nanoparticles. *Science* **2019**, *363* (6430), 959–964.

[23] Jin, Z.; Lv, J.; Jia, H.; Liu, W.; Li, H.; Chen, Z.; Lin, X.; Xie, G.; Liu, X.; Sun, S.; Qiu, H.-J. Nanoporous Al-Ni-Co-Ir-Mo High-Entropy Alloy for Record-High Water Splitting Activity in Acidic Environments. *Small* **2019**, *15* (47), 1904180.

[24] Cai, Z.-X.; Goou, H.; Ito, Y.; Tokunaga, T.; Miyauchi, M.; Abe, H.; Fujita, T. Nanoporous Ultra-High-Entropy Alloys Containing Fourteen Elements for Water Splitting Electrocatalysis. *Chem. Sci.* **2021**, *12* (34), 11306–11315.

[25] Zhu, H.; Zhu, Z.; Hao, J.; Sun, S.; Lu, S.; Wang, C.; Ma, P.; Dong, W.; Du, M. High-Entropy Alloy Stabilized Active Ir for Highly Efficient Acidic Oxygen Evolution. *Chem. Eng. J.* **2022**, *431*, 133251.

[26] Yu, Y.; Li, H.; Liu, J.; Xu, W.; Zhang, D.; Xiong, J.; Li, B.; Omelchuk, A. O.; Lai, J.; Wang, L. High Entropy Stabilizing Lattice Oxygen Participation of Ru- Based Oxides in Acidic Water Oxidation. *J. Mater. Chem. A* **2022**, *10* (40), 21260–21265.

[27] Cai, C.; Xin, Z.; Zhang, X.; Cui, J.; Lv, H.; Ren, W.; Gao, C.; Cai, B. Facile Synthesis of FeCoNiCuIr High Entropy Alloy Nanoparticles for Efficient Oxygen Evolution Electrocatalysis. *Catalysts* **2022**, *12* (9), 1050.

[28] Mei, Y.; Feng, Y.; Zhang, C.; Zhang, Y.; Qi, Q.; Hu, J. High-Entropy Alloy with Mo-Coordination as Efficient Electrocatalyst for Oxygen Evolution Reaction. *ACS Catal.* **2022**, *12* (17), 10808–10817.

[29] Shen, H.; Gracia-Espino, E.; Wang, L.; Qin, D.; Gao, S.; Mamat, X.; Ren, W.; Wagberg, T.; Hu, G. Microwave-Assisted Synthesis of Multimetal Oxygen-Evolving Catalysts. *Electrochem. Commun.* **2017**, *81*, 116–119.

[30] Yao, Y.; Huang, Z.; Xie, P.; Lacey, S. D.; Jacob, R. J.; Xie, H.; Chen, F.; Nie, A.; Pu, T.; Rehwoldt, M.; Yu, D.; Zachariah, M. R.; Wang, C.; Shahbazian-Yassar, R.; Li, J.; Hu, L. Carbothermal Shock Synthesis of High-Entropy-Alloy Nanoparticles. *Science* **2018**, *359* (6383), 1489–1494.

[31] Xu, S.; Zhong, G.; Chen, C.; Zhou, M.; Kline, D. J.; Jacob, R. J.; Xie, H.; He, S.; Huang, Z.; Dai, J.; Brozena, A. H.; Shahbazian-Yassar, R.; Zachariah, M. R.; Anlage, S. M.; Hu, L. Uniform, Scalable, High-Temperature Microwave Shock for Nanoparticle Synthesis through Defect Engineering. *Matter* **2019**, *1* (3), 759–769.

[32] Zhong, G.; Xu, S.; Cui, M.; Dong, Q.; Wang, X.; Xia, Q.; Gao, J.; Pei, Y.; Qiao, Y.; Pastel, G.; Sunaoshi, T.; Yang, B.; Hu, L. Rapid, High-Temperature, In Situ Microwave Synthesis of Bulk Nanocatalysts. *Small* **2019**, *15* (47), 1904881.

[33] Yeh, J.-W.; Chen, S.-K.; Lin, S.-J.; Gan, J.-Y.; Chin, T.-S.; Shun, T.-T.; Tsau, C.-H.; Chang, S.-Y. Nanostructured High-Entropy Alloys with Multiple Principal Elements: Novel Alloy Design Concepts and Outcomes. *Adv. Eng. Mater.* **2004**, *6* (5), 299–303.

[34] Pi, Y.; Shao, Q.; Wang, P.; Guo, J.; Huang, X. General Formation of Monodisperse IrM (M = Ni, Co, Fe) Bimetallic Nanoclusters as Bifunctional Electrocatalysts for Acidic Overall Water Splitting. *Adv. Funct. Mater.* **2017**, *27* (27), 1700886.

[35] Feng, J.; Lv, F.; Zhang, W.; Li, P.; Wang, K.; Yang, C.; Wang, B.; Yang, Y.; Zhou, J.; Lin, F.; Wang, G.-C.; Guo, S. Iridium-Based Multimetallic Porous Hollow Nanocrystals for Efficient Overall-Water-Splitting Catalysis. *Adv. Mater.* **2017**, *29* (47), 1703798.

[36] Park, J.; Sa, Y. J.; Baik, H.; Kwon, T.; Joo, S. H.; Lee, K. Iridium-Based Multimetallic Nanoframe@Nanoframe Structure: An Efficient and Robust Electrocatalyst toward Oxygen Evolution Reaction. *ACS Nano* **2017**, *11* (6), 5500–5509.

[37] Fu, L.; Zeng, X.; Cheng, G.; Luo, W. IrCo Nanodendrite as an Efficient Bifunctional Electrocatalyst for Overall Water Splitting under Acidic Conditions. *ACS Appl. Mater. Interfaces* **2018**, *10* (30), 24993–24998.

[38] Wang, Y.; Zhang, L.; Yin, K.; Zhang, J.; Gao, H.; Liu, N.; Peng, Z.; Zhang, Z. Nanoporous Iridium-Based Alloy Nanowires as Highly Efficient Electrocatalysts Toward Acidic Oxygen Evolution Reaction. *ACS Appl. Mater. Interfaces* **2019**, *11* (43), 39728–39736.

[39] Li, Y.; Xing, L.; Yu, D.; Libanori, A.; Yang, K.; Sun, J.; Nashalian, A.; Zhu, Z.; Ma, Z.; Zhai, Y.; Chen, J. Hollow IrCo Nanoparticles for High-Performance Overall Water Splitting in an Acidic Medium. *ACS Appl. Nano Mater.* **2020**, *3* (12), 11916–11922.

[40] Liu, D.; Lv, Q.; Lu, S.; Fang, J.; Zhang, Y.; Wang, X.; Xue, Y.; Zhu, W.; Zhuang, Z. IrCuNi Deeply Concave Nanocubes as Highly Active Oxygen Evolution Reaction Electrocatalyst in Acid Electrolyte. *Nano Lett.* **2021**, *21* (7), 2809–2816.

[41] McCrory, C. C. L.; Jung, S.; Ferrer, I. M.; Chatman, S. M.; Peters, J. C.; Jaramillo, T. F. Benchmarking Hydrogen Evolving Reaction and Oxygen Evolving Reaction Electrocatalysts for Solar Water Splitting Devices. *J. Am. Chem. Soc.* **2015**, *137* (13), 4347–4357.

[42] McCrory, C. C. L.; Jung, S.; Peters, J. C.; Jaramillo, T. F. Benchmarking Heterogeneous Electrocatalysts for the Oxygen Evolution Reaction. *J. Am. Chem. Soc.* **2013**, *135* (45), 16977–16987.

[43] Seitz, L. C.; Dickens, C. F.; Nishio, K.; Hikita, Y.; Montoya, J.; Doyle, A.; Kirk, C.; Vojvodic, A.; Hwang, H. Y.; Norskov, J. K.; Jaramillo, T. F. A Highly Active and Stable $IrO_x/SrIrO_3$ Catalyst for the Oxygen Evolution Reaction. *Science* **2016**, *353* (6303), 1011–1014.

[44] Tong, X.; Zhang, J.; Zhang, G.; Wei, Q.; Chenitz, R.; Claverie, J. P.; Sun, S. Ultrathin Carbon-Coated Pt/Carbon Nanotubes: A Highly Durable Electrocatalyst for Oxygen Reduction. *Chem. Mater.* **2017**, *29* (21), 9579–9587.

[45] Ji, S. G.; Kwon, H. C.; Kim, T.-H.; Sim, U.; Choi, C. H. Does the Encapsulation Strategy of Pt Nanoparticles with Carbon Layers Really Ensure Both Highly Active and Durable Electrocatalysis in Fuel Cells? *ACS Catal.* **2022**, *12* (12), 7317–7325.

[46] Song, B.; Yang, Y.; Rabbani, M.; Yang, T. T.; He, K.; Hu, X.; Yuan, Y.; Ghildiyal, P.; Dravid, V. P.; Zachariah, M. R.; Saidi, W. A.; Liu, Y.; Shahbazian-Yassar, R. In Situ Oxidation Studies of High-Entropy Alloy Nanoparticles. *ACS Nano* **2020**, *14* (11), 15131–15143.

[47] Song, B.; Yang, Y.; Yang, T. T.; He, K.; Hu, X.; Yuan, Y.; Dravid, V. P.; Zachariah, M. R.; Saidi, W. A.; Liu, Y.; Shahbazian-Yassar, R. Revealing High-Temperature Reduction Dynamics of High-Entropy Alloy Nanoparticles via In Situ Transmission Electron Microscopy. *Nano Lett.* **2021**, *21* (4), 1742–1748.

[48] Spanos, I.; Auer, A. A.; Neugebauer, S.; Deng, X.; Tüysüz, H.; Schlögl, R. Standardized Benchmarking of Water Splitting Catalysts in a Combined Electrochemical Flow Cell/Inductively Coupled Plasma–Optical Emission Spectrometry (ICP-OES) Setup. *ACS Catal.* **2017**, *7* (6), 3768–3778.

[49] Nong, H. N.; Gan, L.; Willinger, E.; Teschner, D.; Strasser, P. IrO_x Core-Shell Nanocatalysts for Cost- and Energy-Efficient Electrochemical Water Splitting. *Chem. Sci.* **2014**, *5* (8), 2955–2963.

[50] Reier, T.; Pawolek, Z.; Cherevko, S.; Bruns, M.; Jones, T.; Teschner, D.; Selve, S.; Bergmann, A.; Nong, H. N.; Schlögl, R.; Mayrhofer, K. J. J.; Strasser, P. Molecular Insight in Structure and Activity of Highly Efficient, Low-Ir Ir–Ni Oxide Catalysts for Electrochemical Water Splitting (OER). *J. Am. Chem. Soc.* **2015**, *137* (40), 13031–13040.

[51] Shan, J.; Ye, C.; Chen, S.; Sun, T.; Jiao, Y.; Liu, L.; Zhu, C.; Song, L.; Han, Y.; Jaroniec, M.; Zhu, Y.; Zheng, Y.; Qiao, S.-Z. Short-Range Ordered Iridium Single Atoms Integrated into Cobalt Oxide Spinel Structure for Highly Efficient Electrocatalytic Water Oxidation. *J. Am. Chem. Soc.* **2021**, *143* (13), 5201–5211.

[52] Sandbeck, D. J. S.; Inaba, M.; Quinson, J.; Bucher, J.; Zana, A.; Arenz, M.; Cherevko, S. Particle Size Effect on Platinum Dissolution: Practical Considerations for Fuel Cells. *ACS Appl. Mater. Interfaces* **2020**, *12* (23), 25718–25727.

[53] Oh, H.-S.; Nong, H. N.; Reier, T.; Bergmann, A.; Gliech, M.; Ferreira de Araújo, J.; Willinger, E.; Schlögl, R.; Teschner, D.; Strasser, P. Electrochemical Catalyst–Support Effects and Their Stabilizing Role for IrO_x Nanoparticle Catalysts during the Oxygen Evolution Reaction. *J. Am. Chem. Soc.* **2016**, *138* (38), 12552–12563.

[54] Nong, H. N.; Reier, T.; Oh, H.-S.; Gliech, M.; Paciok, P.; Vu, T. H. T.; Teschner, D.; Heggen, M.; Petkov, V.; Schlögl, R.; Jones, T.; Strasser, P. A Unique Oxygen Ligand Environment Facilitates Water Oxidation in Hole-Doped $IrNiO_x$ Core–Shell Electrocatalysts. *Nat. Catal.* **2018**, *1* (11), 841–851.

[55] Kasian, O.; Grote, J.-P.; Geiger, S.; Cherevko, S.; Mayrhofer, K. J. J. The Common Intermediates of Oxygen Evolution and Dissolution Reactions during Water Electrolysis on Iridium. *Angew. Chem. Int. Ed.* **2018**, *57* (9), 2488–2491.

[56] Li, H.; Zhu, H.; Shen, Q.; Huang, S.; Lu, S.; Ma, P.; Dong, W.; Du, M. A Novel Synergistic Confinement Strategy for Controlled Synthesis of High-Entropy Alloy Electrocatalysts. *Chem. Commun.* **2021**, *57* (21), 2637–2640.

Supporting Information:

Experimental section; HAADF-STEM images, HR-TEM images, and STEM-EDX analysis of IrFeCoNiCu-HEA catalysts; ICP-OES analysis of IrFeCoNiCu-HEA and dissolved metals in the electrolyte; XRD patterns of Ir-based bimetallic catalysts and post-electrolysis IrFeCoNiCu-HEA; ECSA analysis of Ir and IrFeCoNiCu-HEA; STEM-EELS maps of post-electrolysis IrFeCoNiCu-HEA; and XPS spectra of IrFeCoNiCu-HEA.

Acknowledgments:

This work was financially supported by the BASF CARA program (No. 88622627). Work at the Molecular Foundry was supported by the Office of Science, Office of Basic Energy Sciences of the U.S. Department of Energy under Contract No. DE-AC02-05CH11231. P.-C.C. acknowledges support from Kavli ENSI Heising-Simons Fellowship. Y.Y. acknowledges support from Miller Fellowship.

Competing Interests:

The Authors declare no competing financial interests.

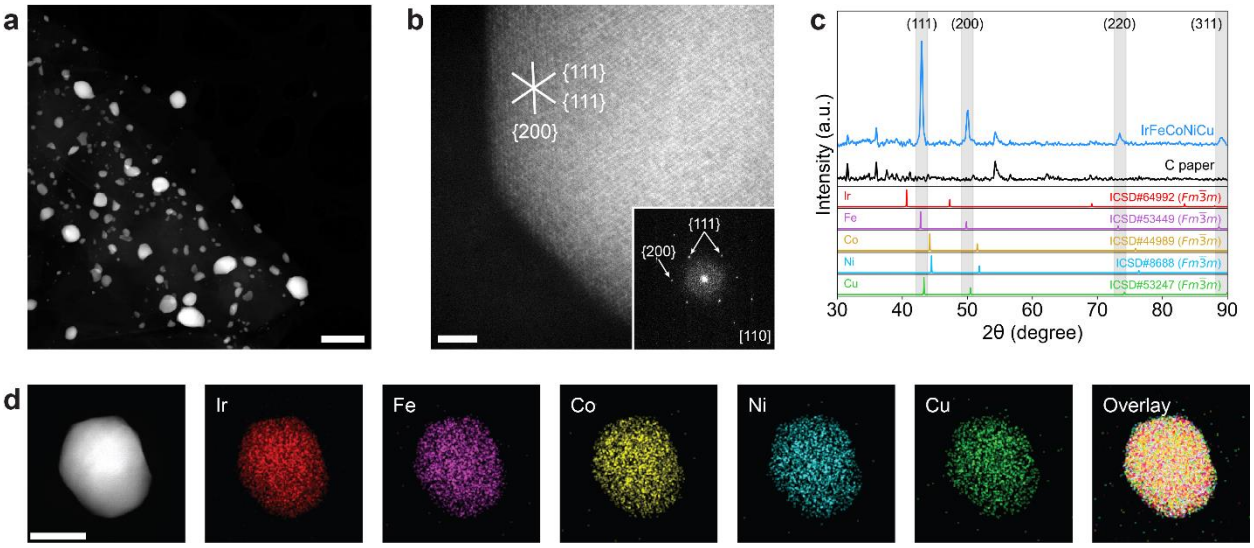

Figure 1. (a) Low-resolution HAADF-STEM image of IrFeCoNiCu-HEA dispersed on carbon paper substrate (scale bar, 500 nm). **(b)** High-resolution HAADF-STEM image (scale bar, 2 nm) and inset of the corresponding FFT showing a typical FCC structure. **(c)** XRD pattern of IrFeCoNiCu-HEA showing the single-phase FCC structure. **(d)** Homogeneous elemental distribution of IrFeCoNiCu-HEA showed by individual and overlay STEM-EDX maps (scale bar, 50 nm).

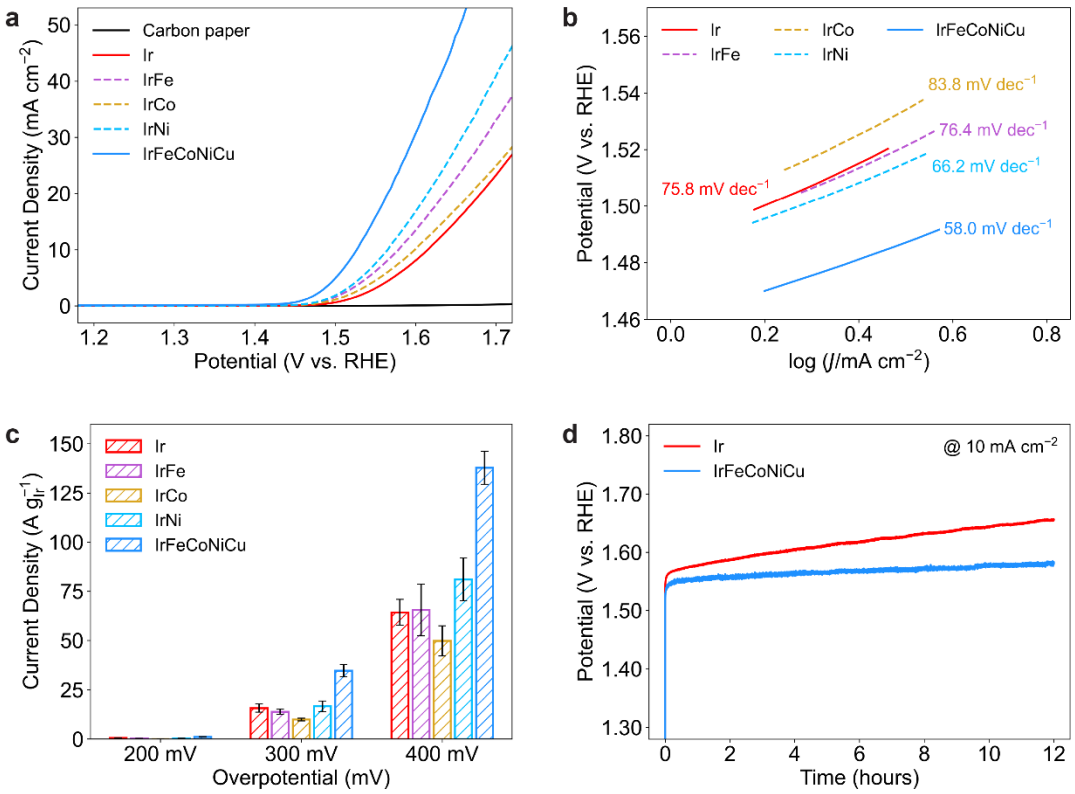

Figure 2. (a) OER polarization curves in 0.1 M $HClO_4$ electrolyte (scan rate, 5 mV s^{-1}). **(b)** Corresponding Tafel slope. **(c)** Ir-mass-based activity measured at different overpotentials. **(d)** Chronopotentiometry measurement at a constant current density of 10 mA cm^{-2}.

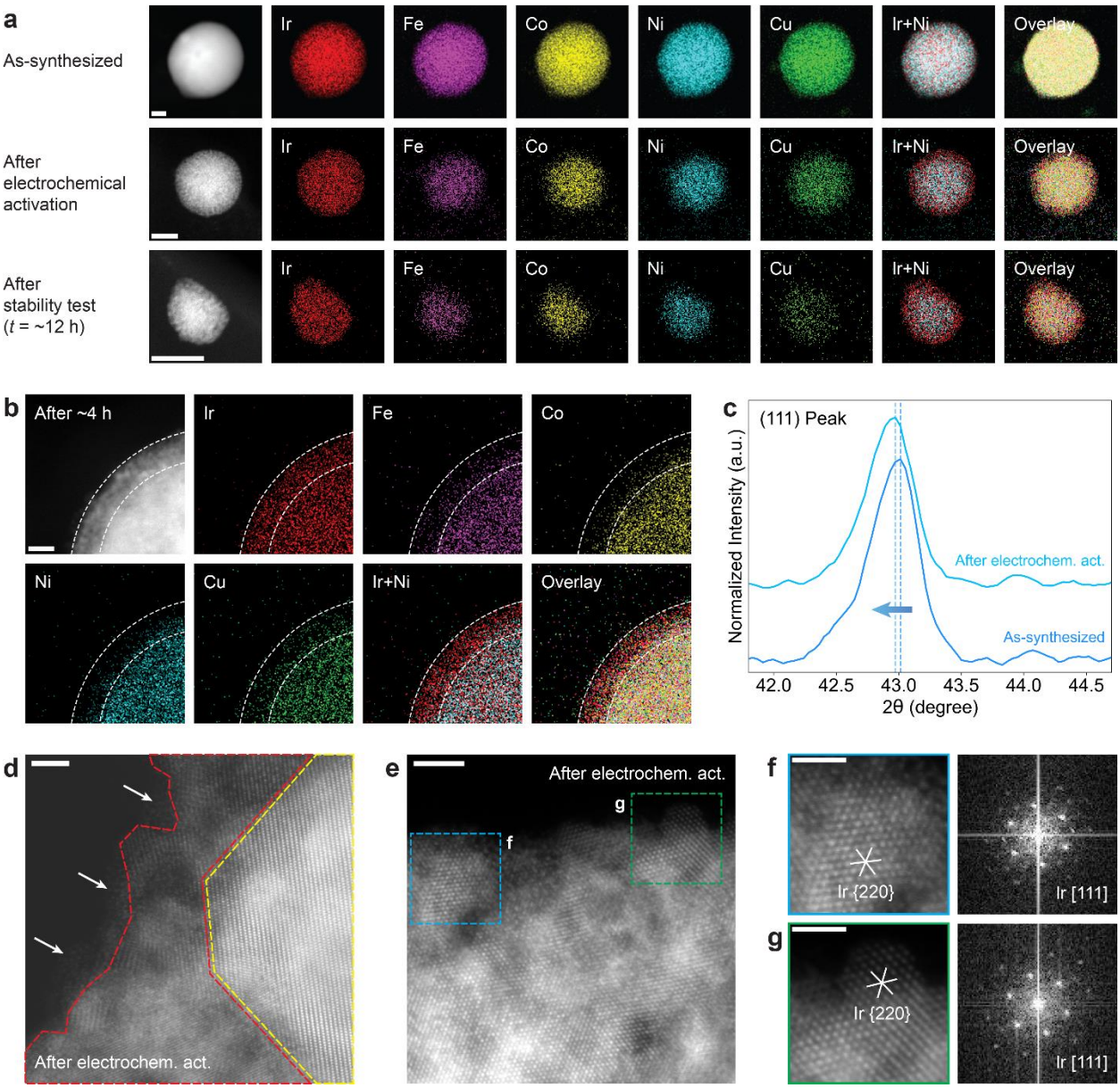

470 **Figure 3. (a)** STEM-EDX maps showing the elemental distribution of IrFeCoNiCu-HEA at different time points of the OER stability test (all scale bar, 20 nm). **(b)** STEM-EDX maps showing the Ir-rich shell layer near the surface of the nanoparticle, as highlighted by the dashed lines (scale bar, 10 nm). **(c)** Comparison of the (111) peaks from powder XRD measurement between as-synthesized and post-electrocatalysis samples showing a slight peak shift. **(d)** Near-surface structure of the nanoparticle showing the HEA core, 475 polycrystalline alloy shell layer (~2-6 nm), and surface oxide (indicated by white arrows) after electrochemical activation. **(e)** HAADF-STEM image of IrFeCoNiCu-HEA near the surface showing the Ir-rich nano-domains (scale bar, 2 nm). **(f-g)** Ir domains populate the shell layer and surface of the nanoparticle, having different in-plane rotational angles (all scale bar, 1 nm).

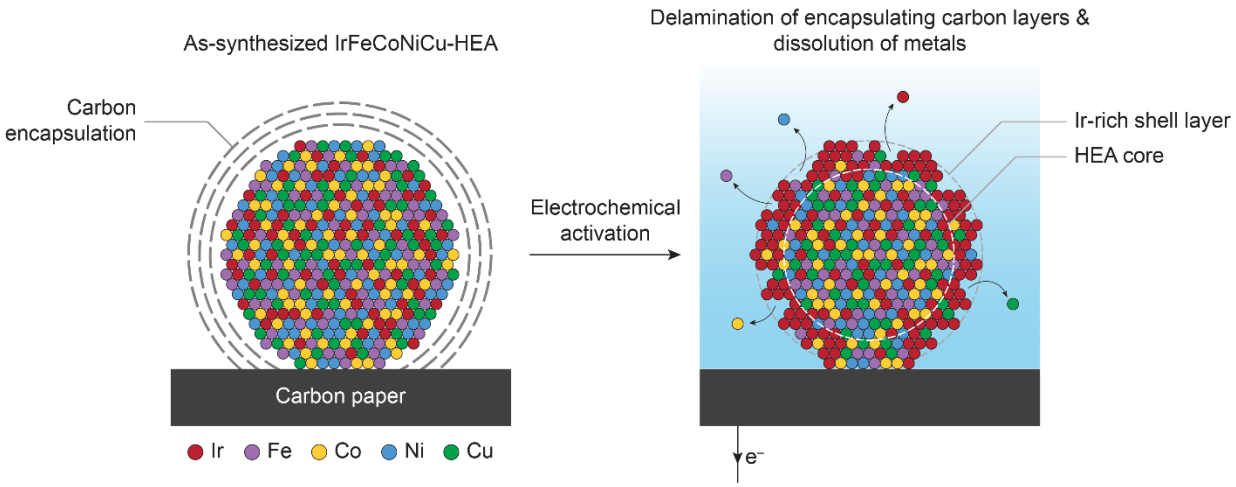

Figure 4. Illustration of the structural evolution of IrFeCoNiCu-HEA nanoparticle under acidic OER conditions. The electrocatalytic condition induces delamination of the encapsulating carbon layers and dissolution of mostly the 3*d* metals, leaving an Ir-rich shell layer on the surface of the nanoparticle.

TOC Graphic:

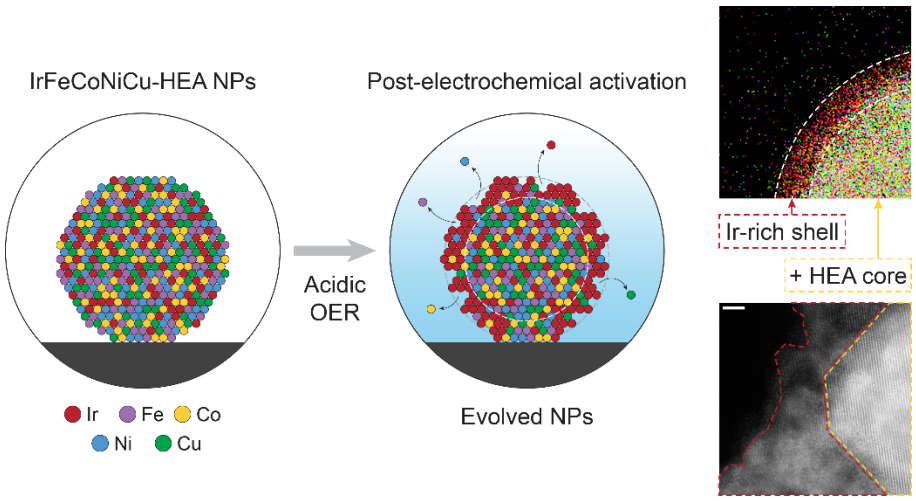

485